Nanoscaled Fractal Superstructures via Laser Patterning—A Versatile Route to Metallic Hierarchical Porous Materials

Hendrik Reinhardt, Moritz Kroll, Sarah L. Karstens, Sabine Schlabach, Norbert A. Hampp,* and Ulrich Tallarek*

A laser-based procedure for the preparation of metallic hierarchical porous materials is introduced and exemplified on tin, copper, silicon, titanium, and tungsten surfaces to demonstrate its general applicability. The impact of suitably tuned nanosecond laser pulses triggers a process in which laser-induced metal ablation and instantaneous recondensation of partially oxidized metals lead to cauliflower-like superstructures comprising a hybrid micro-/nanopatterning. Repeated scanning with the intense focused beam over the surface creates microstructures of hierarchically tunable porosity in a layer-by-layer design. The 3D morphology of these superstructures is analyzed using tomographic data based on focused ion-beam scanning electron microscopy to return a fractal dimension of $D_f = 2.79$—practically identical to a natural cauliflower ($D_f \approx 2.8$), even though the plant is four orders of magnitude larger than the superstructures generated through the laser process. The high D_f value signifies a complex morphology that boasts a huge external surface. The introduced concept enables convenient access to a variety of metallic hierarchical porous materials, which are key to performance in environmentally and technologically relevant areas like energy generation, storage, and conversion, as well as sensing and catalysis.

1. Introduction

Hierarchical porous materials (HPMs) attract increasing attention as they combine the benefits of nanomaterials with enhanced mechanical robustness and structural integrity.[1,2] Multilevel porosity on the scale of micro-, meso-, and macropores is a common characteristic of this intriguing class of functional materials.[3] Their interconnected hierarchical porosity provides large specific surface area and huge accessible pore volume, which are favorable in fundamental processes, such as light harvesting, charge carrier transport, and mass diffusion.[4] Currently, the applications for HPMs range from (photo)catalysis[5,6] via energy storage[7–9] and conversion[10,11] to separation,[12,13] sensing,[14,15] and pollution remediation.[16] At first glance, nanoparticles appear as ideal candidates for such applications, however, in practice nanoparticles tend to agglomerate, leading to the loss of active surface area and hence reduced performance. This problem can be overcome by materials comprising microstructures that carry nanopatterns such that aggregation is avoided and the active surface preserved.

A natural example that demonstrates the great potential of HPMs is the lotus leaf.[17] Its upper side is covered by microsized papillae which secrete nanostructured waxy substances. The self-cleaning ability of the lotus leaf inspired lasting efforts in creating mimicry for technical implementations. Besides water conservation, applications include anti-icing, antifogging, and corrosion protection.[18] HPMs in general promise a boost of performance for many applications where a high specific surface area is essential. A major hurdle for rapid progress, however, is the lack of a universal synthesis route for HPMs applicable to a wide range of materials. Established approaches, such as templating strategies, solvothermal synthesis, the sol–gel method, and selective leaching are material-specific and thus not generally applicable.[19] With regard to versatility and sustainability, laser-based processes are well suited as they are readily applicable to a multitude of materials, easy to reproduce, solvent-free, and scalable. Although commonly perceived as tools for micropatterning, lasers are increasingly used for nanostructure formation. Examples include laser-induced periodic surface structures,[20,21] pulsed laser-induced dewetting,[22,23] and formation of nanocomposites via laser-stimulated self-organization.[24,25] To enhance the specific surface area of solids, femtosecond lasers are often used, since they facilitate the ablation of almost any material, thus roughening its surface.[26,27]

Dr. H. Reinhardt, M. Kroll, S. L. Karstens, Prof. N. A. Hampp,
Prof. U. Tallarek
Department of Chemistry
Philipps-Universität Marburg
Hans-Meerwein-Strasse 4, Marburg 35032, Germany
E-mail: hampp@staff.uni-marburg.de; tallarek@staff.uni-marburg.de
Dr. S. Schlabach
Institute for Applied Materials (IAM) and Karlsruhe Nano
Micro Facility (KNMF)
Karlsruhe Institute of Technology
Eggenstein-Leopoldshafen 76344, Germany

The ORCID identification number(s) for the author(s) of this article can be found under https://doi.org/10.1002/admi.202000253.
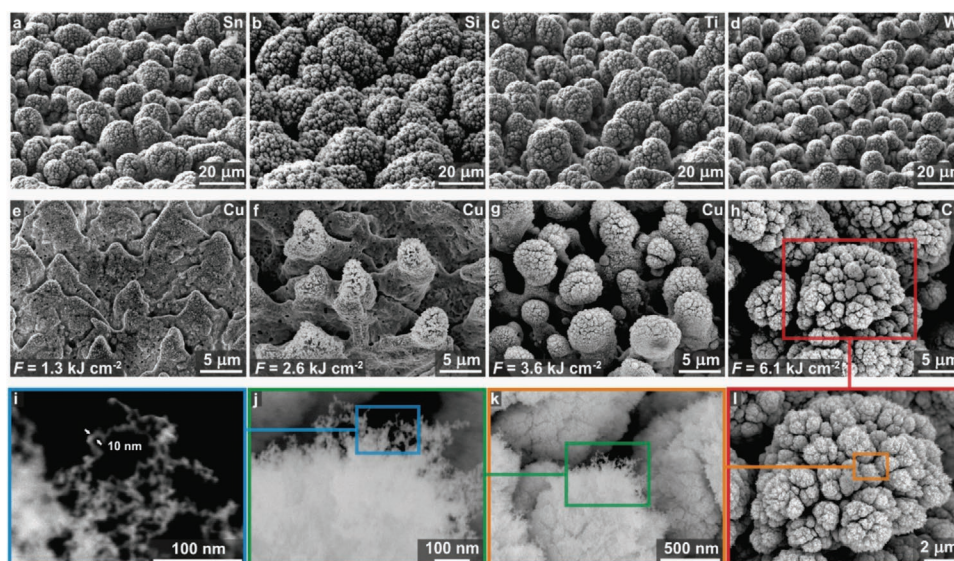
Figure 1. Laser-induced formation of HPMs on a) tin, b) silicon, c) titanium, and d) tungsten. e–h) Electron micrographs visualizing the pattern formation on copper in dependence of the laser fluence *F*. i–l) Detailed views on the nanostructure of a copper cauliflower (with increasing magnification from right to left).

This study introduces a laser-based concept for the generation of metallic HPMs. Despite the current trend of using femtosecond lasers for surface patterning, the advantage of nanosecond lasers for this field of application is demonstrated. As the names suggest, the primary difference between the two laser types is the pulse duration. Laser pulses in the femtosecond time domain are well suited for pure ablation since the thermalization time of materials scales in the picosecond domain. In addition to ablation, nanosecond lasers induce photothermal heating of the treated materials because their pulse duration surpasses the time required for thermalization. Concomitant heating during pattern formation offers control over the morphology and composition during the patterning process. The demonstrated technique is based on photothermal heat accumulation on the metallic surfaces beyond the point of evaporation. It facilitates reactions between the affected materials and the surrounding medium (in this case ambient air) into which a recondensation zone is expanding. Rapid quenching leads to the recondensation of reaction products that form highly porous nanostructures on self-organized microstructures. The very interaction of these micro- and nanostructuring effects facilitates formation of HPMs from a variety of metals. The composition of these HPMs may be controlled by specific reactive environments for quenching recondensation. To demonstrate the general applicability of this concept, materials with pronounced differences in their melting and evaporation temperatures (Sn, Cu, Si, Ti, and W) were transformed into HPMs (**Figure 1**). All laser treatments were conducted in ambient air, consequently resulting in oxidic HPMs. Using copper as example, the mechanisms of nanosecond laser-induced HPM generation are disclosed. In order to elucidate the formation process of the laser-generated cauliflower-like superstructures, their 3D morphology is analyzed using focused ion-beam scanning electron microscopy (FIB-SEM).

2. Results and Discussion

Laser-generated HPMs on tin (Sn), silicon (Si), titanium (Ti), and tungsten (W) are shown in Figure 1a–d. The wide span of melting points underlines the general applicability of nanosecond laser-based HPM formation. The mechanism of hierarchical pattern formation is illustrated in more detail using copper (Cu) as example. Its melting point is right between Sn and Si. Hybrid patterning of copper sheets was conducted with a 532 nm nanosecond pulsed laser having a pulse width of 6 ns. For the modification of extended surface area, the laser beam was focused to a spot diameter of 30 μm and scanned over the copper samples in a meandering motion with a line spacing of 5 μm. Both pulse energy and pulse frequency were kept constant at 90 μJ and 50 kHz, respectively. Depending on the line scan speed of the laser spot, affected surface areas were subjected to a specific energy input per unit area, henceforth indicated as laser fluence *F*. At a comparably low *F* of 1.3 kJ cm^{-2}, the copper surface is initially transformed into a scaly texture (Figure 1e). When *F* is doubled, bud-like microstructures with diameters around 5 μm appear (Figure 1f). A further increase to *F* = 3.6 kJ cm^{-2} yields a surface morphology that shares similarities with the lotus leaf (Figure 1g). Finally, at a laser fluence of 6.1 kJ cm^{-2}, cauliflower-like structures are generated (Figure 1h). These are composed of conically shaped subunits. The most striking feature of these cauliflower-like structures are delicate nanostructures that can hardly be resolved even by high resolution SEM (Figure 1i–l). The copper surfaces modified with cauliflowers appear night-black and exhibit broadband absorption in a wavelength range of 200–2500 nm (Section S1, Supporting Information). This is attributed less to the type of material the cauliflowers are made of (Cu_2O and CuO; Section S2, Supporting Information) but rather to light getting trapped in their fuzzy surface architecture. Hence, the question arises how structures of such complexity are actually formed.
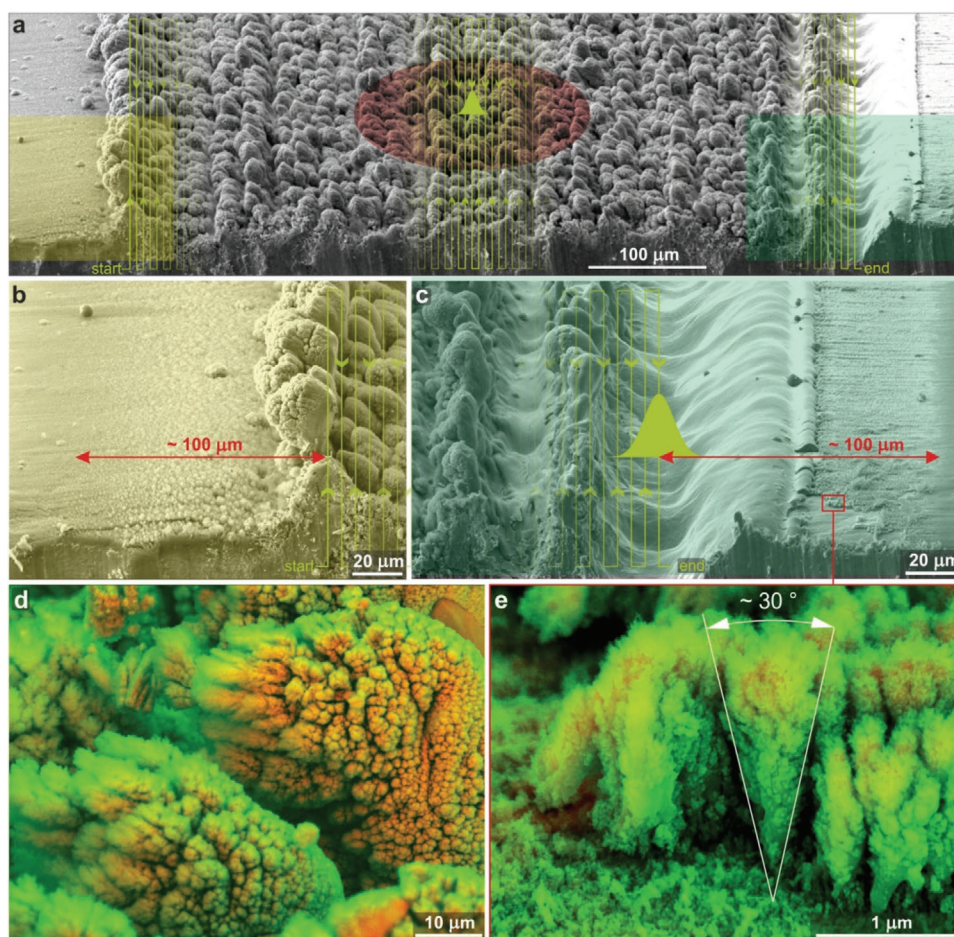
2000253 (2 of 7)

**ADVANCED
SCIENCE NEWS**

www.advancedsciencenews.com

**ADVANCED
MATERIALS
INTERFACES**

www.advmatinterfaces.de

Figure 2. Mechanisms of laser-induced hybrid patterning. a) Perspective view onto a cauliflower field formed with a laser fluence of 7 kJ cm^{-2} on copper. The meandering path of the laser spot is marked by green lines and is true-to-scale (line spacing, 5 μm). In the center, the size of the laser spot is represented by its Gaussian intensity distribution. The surrounding red colored region marks the spatial expansion of the recondensation zone ($r = 100$ μm). b,c) Detailed views on the highlighted start and end zones of the cauliflower field. Deposition radius (red arrows), spot path (green lines), and laser intensity profile are superimposed. d) Cauliflowers in the field visualized by interlacing morphology (green, secondary electron detector) and material contrast (orange, backscattered electron detector). e) Electron micrograph of nanomaterial deposits found on the right side of the cauliflower field (end of the laser scan).

Investigation of a field of cauliflowers provides insight into the process of hybrid micro-/nanostructure formation (**Figure 2**a). The laser spot was scanned along a meandering path from left to right, as indicated by the superimposed green lines.

Intriguingly, microstructures resulting from the laser treatment are larger than the line spacing of the laser scans, which are displayed true-to-scale (5 μm line spacing). The reason why structures larger than the scan line spacing are created becomes clear at the right edge of the scanned field. At the applied laser fluence (7 kJ cm^{-2} in this case) copper is not ablated homogeneously but is rather transformed into microstructures which, due to their geometry, avoid annihilation under the intense laser irradiation. Besides ablation, nanosecond laser pulses also induce photothermal heating which leads to a softening of the generated microstructures. This enables mass transport away from the heat source, thus causing the observed convergence of microstructures adjacent to already solidified ones. Like surging waves, the microstructures are added row by row. Intense laser irradiation also leads to the evaporation of copper, thereby creating a recondensation zone (cf. Figure 2a),

out of which reaction products between copper and oxygen (the laser process was conducted in air) recondense in a radius of ≈100 μm around the laser spot, as the deposition fringes in Figure 2b,c illustrate. It is striking that all microstructures feature an orientation-dependent coverage with copper oxides (Figure 2d). Sides facing the laser-induced recondensation zone exhibit fewer deposits compared to sides remaining unaffected by scattered laser light. Hence, the formation of the nanostructures is a process comprising deposition and deterioration, or rather, melting. Lasting nanostructures are deposited over a distance of up to ≈50 μm from the recondensation zone center. With increasing distance, mutual shadowing of the hybrid structures provides protection against scattered laser light and radiated heat. The overall course of the structural evolution is recapitulated in **Figure 3**. In the very first laser scan the copper surface is just slightly roughened. As a result, photothermal coupling is improved, promoting distinct morphological transformations to occur upon the second and all subsequent laser scans. Microstructures created in this process accumulate to fields as described above and mature into cauliflowers as soon
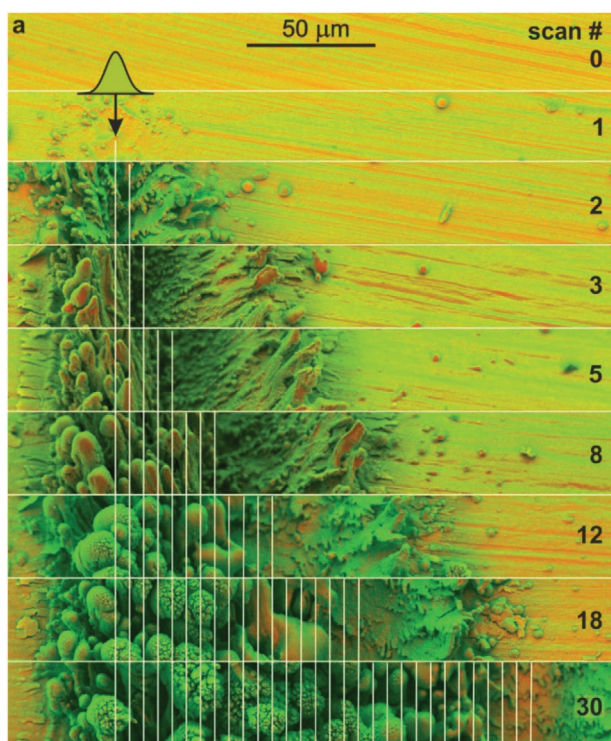
Figure 3. Sequential view of hybrid pattern formation. Series of assembled electron micrographs illustrating the course of pattern formation on copper at a laser fluence of 6.1 kJ cm^{-2}. The number of applied scans is indicated on the right (line spacing, 5 µm).

as nanostructure build-up overcomes nanostructure deterioration inflicted by radiation damage. In the literature, similar SnO$_2$ structures have been observed for layer deposited gasborn particles synthesized in a microwave plasma process.[28,29] This shows that highly porous structures can be produced by recondensation processes, in general.

Investigations into the inner structure of resulting cauliflowers substantiate a formation process based on layer-by-layer deposition of reaction products recondensing onto microstructures created by the earlier scan(s) (**Figure 4**a). The studies of Kask et al.,[30] Vlasova et al.,[31] and Aksenov et al.[32] provide detailed insights

into fractal pattern formation in and around laser plasmas. The cross-sectional view onto a FIB-sliced cauliflower reveals that early deposits fuse due the close proximity to the recondensation zone center. With increasing distance to this hotspot, the balance is increasingly shifted toward nanostructure build-up. The number of superimposed porous layers can be controlled by the line spacing of the laser scan pattern. Halving the spacing to 2.5 µm, for instance, results in twice the number of deposited layers since the microstructures are passed by the recondensation zone twice as often (Figure 4b). Similar to tree rings, the history of structure formation can therefore be traced in detail.

To provide detailed insights into the 3D pore space morphology, the copper cauliflower shown in Figure 4a was reconstructed from data obtained by FIB-SEM tomography (**Scheme 1** and **Figure 5**a). The fractal nature of the solid phase as well as the spatial and size distributions of macroporous void space were analyzed based on the binarized tomographic data. Cauliflower cross-sections in Figure 4a,b suggest that the morphology of solid substructure can be described as fractal with scaling self-similarity. To prove that the laser-generated cauliflowers truly resemble fractals, the box-counting method[33–35] was chosen to determine their fractal dimension D_f (see Section S3, Supporting Information). The box-counting method divides 3D structures into boxes and counts the number of boxes containing solids. The fractal dimension D_f of a structure is determined from the slope of a double-logarithmic plot of the box counts versus the box size. For laser-generated cauliflowers, the plot shows a constant slope of $D_f = 2.79 \pm 0.02$ (Figure 4c). Feature sizes from 0.06 to 1.48 µm are contained within the fractal range. The high value of D_f confirms the complex boundary[34] of the laser-generated cauliflowers and indicates a structure becoming increasingly finer from the center outward, thereby unfolding a huge external surface. Intriguingly, natural cauliflowers have a fractal dimension of $D_f = 2.8$,[36] although the plant is about four orders of magnitude larger than the laser-generated cauliflowers.

To verify the above-mentioned formation process of cauliflowers, the porosity distribution was analyzed. The porosity is described as the fraction of void space in the porous medium and was determined from the ratio of black voxels to the sum of white and black voxels in the binarized reconstruction.
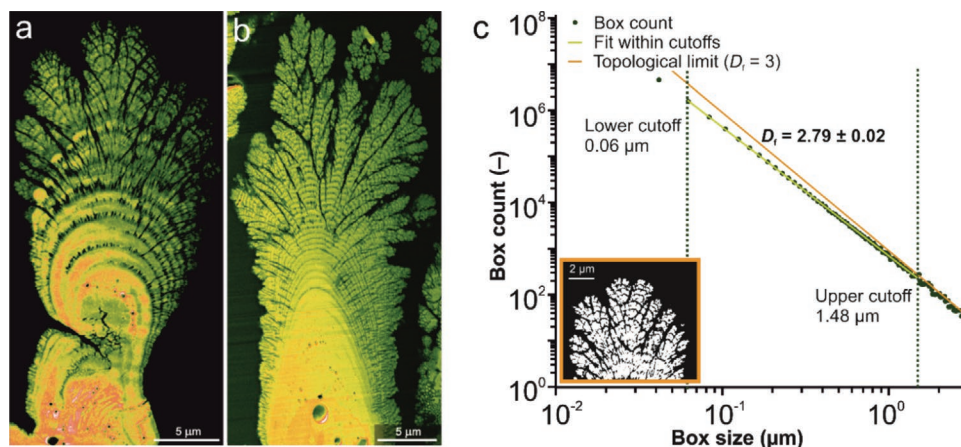

Figure 4. Cross-sections of cauliflowers and fractal analysis. a) Cross-section via FIB slicing of a cauliflower generated with a laser scan line spacing of 5 µm and b) of 2.5 µm. c) Determination of the fractal dimension D_f, providing an index of the space-filling capacity and complexity of a fractal. The inset shows a slice of the 3D volume that was used as input for the analysis.
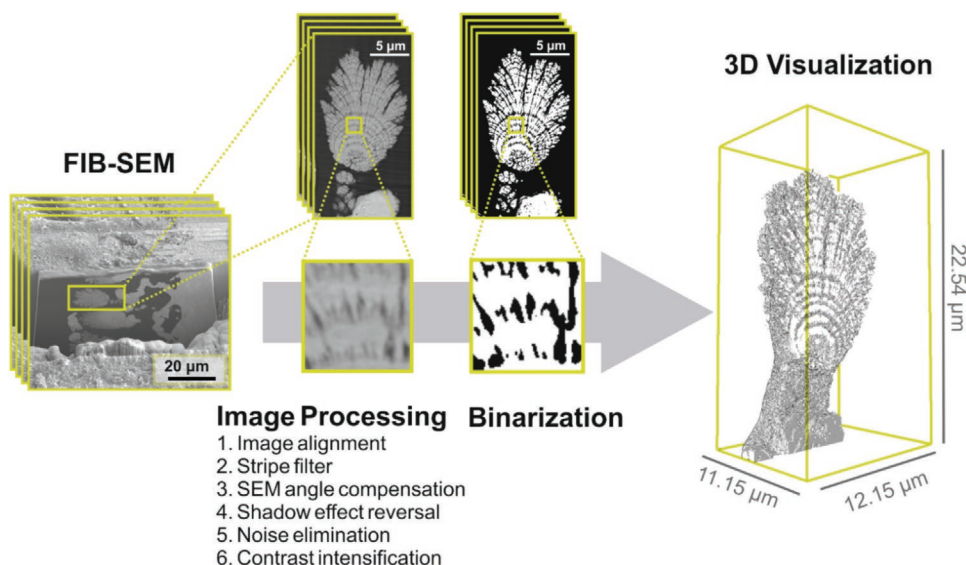
Scheme 1. Overview of the 3D reconstruction workflow based on FIB-SEM.

Accordingly, the global porosity of laser-generated cauliflowers is ≈34%, whereby the proportion of closed pores (predominantly located in the stem) is about 1% (Figure 5b). The closed pores are presumably formed due to the trapping of gas upon rapid solidification of liquid and partially evaporated material as soon as the laser-generated heat zone moves away. With increasing distance to the laser spot, evaporated material recondenses onto the previously generated microstructures. Due to the meandering scan pattern of the laser spot this event is repeated, thus

forming layered deposits piling up to a porous network. The resulting superstructure is shown in Figure 5c together with a plot determining the porosity ε of the deposited layers (cf. Section S3, Supporting Information). All layer contours can be fitted very well using ellipses that share the same center point. Together with a uniform mean layer height of 0.7 ± 0.1 µm (distance between ellipses along the major direction), this corroborates the layer-based growth model established for laser-generated cauliflowers. Slight deviations from the ideal
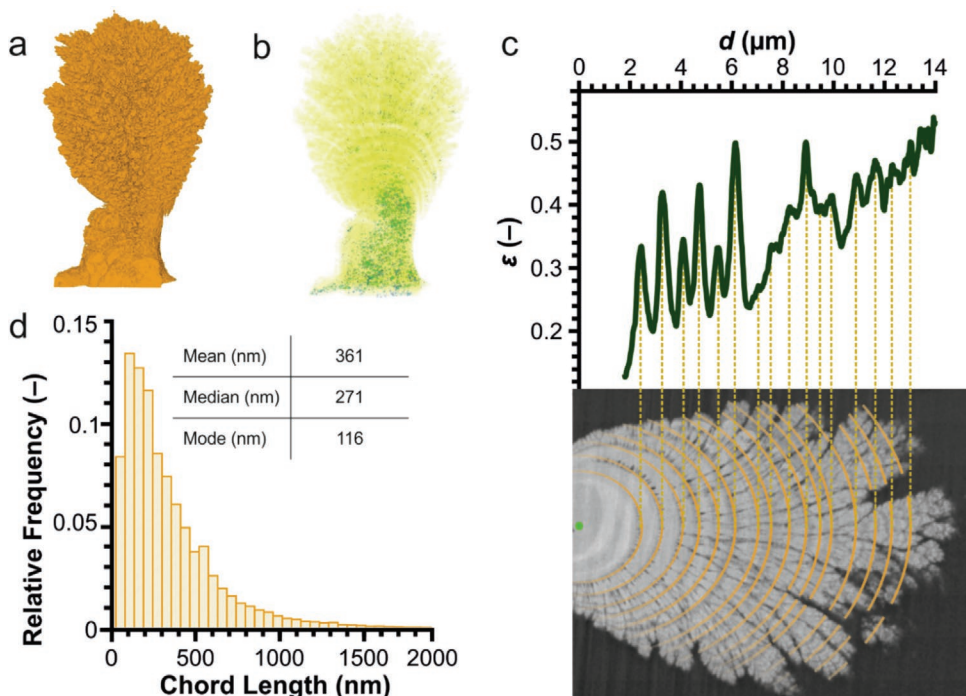

Figure 5. Porosity analysis for a cauliflower reconstructed using FIB-SEM tomography. a) 3D visualization of the reconstructed cauliflower. b) Closed porosity is highlighted in green. c) Porosity profile along elliptical rings (orange) fitting the layered structure of the cauliflower. All ellipses have the same center point (green, left side of the image). Porosity increases from inner to outer layers. d) Characterization of macropore size in the reconstruction by CLD analysis.

ellipsoidal geometry are due to mutual shadowing effects of cauliflowers growing next to each other in the recondensation zone. Alternating peak heights in the porosity plot result from interfaces created by the layer-wise deposition scheme as well as the meandering scan path of the laser spot including changes in direction. Nevertheless, the overall porosity shows a clear increase from the inner elliptical rings to the outer ones, hence the fraction of void space is higher in the outer layers.

To move beyond porosity and characterize the void space regarding its characteristic size, we employed chord length distribution (CLD) analysis (Section S3, Supporting Information).[37–39] In general, the chords collected in a CLD sample the geometry by measuring distances between two interfaces set apart by a homogeneous phase. Since CLD generation does not require any assumptions about the size and shape of the analyzed phase, this methodology is virtually applicable to all multiphase materials. CLD analysis proceeds along the following steps: seed points are randomly placed in the void space of a reconstructed cauliflower; from each point, vectors are projected in angularly equispaced directions until they hit the void-solid interface; finally, chord lengths are extracted as the sum of the absolute lengths of a pair of opposing vectors and stored. The histogram in Figure 5d (the CLD) contains the distribution of chords characterizing the void space of laser-generated cauliflowers. It should be noted that meso- and micropores, which are obviously present in the hierarchically structured cauliflowers (see Figure 1j–l), are not represented in this analysis as they could not be resolved by FIB-SEM tomography. The CLD shows a median pore size of 0.27 μm and a wide distribution of pore sizes ranging from 50 nm up to 2 μm, underlining the fractal nature of the hierarchical pore network. Besides a wide range of envisioned applications, it makes these laser-generated cauliflowers particularly attractive for catalytic networks[40] and electrochemical processes.[41]

3. Conclusion

A universal concept for the generation of metallic HPMs based on a facile nanosecond pulsed laser-treatment of solids is introduced. Using the examples of tin, copper, silicon, titanium, and tungsten the general applicability of the methodology is demonstrated. The process is easy to implement, reproducible, solvent-free, and scalable. The surfaces transformed into HPMs appear deep black, as light is trapped inside the hybrid micro-/nanostructures. The formation process of cauliflower-like superstructures and their morphology was closely investigated. Basically, intense nanosecond laser pulses ablate the surface of solids, while at the same time heating it up to the point of evaporation. Microstructures self-organizing in this regime are simultaneously coated with nanostructured materials from the recondensation zone. Due to the meandering path of the laser scan, material deposition occurs in a layer-by-layer scheme. Fractal superstructures result from a scenario comprising nanostructure build-up and deterioration. The shape and morphology of the generated superstructures are tunable by laser process parameters, such as the line spacing and energy fluence. A cauliflower-like superstructure was analyzed via physical reconstruction based on FIB-SEM tomography.

It features a fractal dimension of 2.79, a value very close to that of natural cauliflowers (2.8). Together with the hybrid micro-/nanostructure patterns, the fractal characteristic of the laser-generated cauliflowers classifies them as HPMs with highly tunable properties, promising potential for a variety of technical applications.

4. Experimental Section

Nanosecond Laser Structuring: All laser treatments were carried out in ambient air using a frequency doubled nanosecond pulsed laser (Spectra Physics Explorer XP 5-532, Newport, Santa Clara, CA) emitting at 532 nm. All specimen materials (Sn, Cu, Si, Ti, W) were modified at an average laser power of 4.5 W, a pulse frequency of 50 kHz, a pulse energy of 90 μJ, and a pulse width of 6 ns. The laser beam was focused to a spot diameter of 30 μm ($1/e^2$) by a 163 mm focal length F-Theta lens (Rhodenstock 163–532, Munich, Germany). The focus spot was scanned over the sample surfaces in a meandering pattern using a galvanometer scan head (ScanGine 14, Scanlab, Puchheim, Germany). For the adjustment of laser fluences F suitable for HPM generation, the scan speed of the laser spot was varied in a range between 5 and 50 mm s^{-1}, while the line spacing was kept constant at 5 μm, unless indicated otherwise.

Scanning Electron Microscopy: SEM was performed on a field emission microscope (JSM-7500F, Jeol, Tokyo, Japan) equipped with a backscattered electron detector for material contrast imaging correlated to the effective atomic number.

Crystal Structure Analysis: Crystal structure analyses were performed on an X'pert PRO MPD (Philips, Eindhoven, The Netherlands) X-ray powder diffractometer equipped with an X'pert tube Co LFF operating at 40 kV and 30 mA. Diffractograms were recorded in a range of 45° ≤ 2Θ ≤ 105° and with an angular resolution of 0.1° 2Θ at room temperature.

FIB-SEM: The morphology of a copper HPM was investigated using tomographic data obtained by a Strata 400S dual-beam FIB-SEM system (FEI/ThermoFisher Scientific, Hillsboro, OR). For that purpose, the pore space of the sample was filled with epoxy resin to enhance contrast and prevent shine-through artifacts as well as redeposition in the pores during serial sectioning. In particular, a 5:2 w/w mixture of SpeciFix resin and SpeciFix-40 curing agent (Struers, Ballerup, Denmark) was used to infiltrate the porous sample under vacuum (<100 mbar). Prior to sectioning, a protective Pt layer was deposited to reduce curtaining effects. The focused beam of Ga$^+$ ions was operated at 30 kV with a current of 6.5 nA to create a trench around the region of interest and to acquire an image stack using the Slice&View package of the instrument software. Image acquisition was performed via SEM at 5 kV using an Everhart–Thornley detector. The final image stack contained 202 slices with (20.8 × 20.8) nm^2 pixel size and 50 nm spacing in milling direction.

Physical Reconstruction: Image restoration and processing were realized with Fiji[42] ImageJ in combination with Visual C# scripts. Images were first aligned to correct drifts between slices. Curtaining effects were eliminated by using the Stripes Filter of the Xlib[43] ImageJ plugin. The inclined SEM viewing angle (52°) was corrected by rescaling the voxels in ImageJ. Intensity gradients within the two phases were normalized in all three spatial directions. Noise was removed by applying a Gaussian filter ($\sigma = 1$). Finally, image contrast was enhanced. In the last step, the image stack was binarized by applying a Phansalkar auto local threshold in ImageJ to distinguish between the bright copper HPM substructure and the dark epoxy resin. Scheme 1 provides an overview of the reconstruction workflow and shows a 3D visualization of a reconstructed copper HPM.

Morphological Analysis: The binary 8-bit image stack was used as input for the morphological analysis. White voxels are treated as solid phase and black voxels as void space. This allows the characterization of the interstitial void space in terms of porosity distribution, mean feature size, and fractal dimension. The underlying computational procedures are described in the Supporting Information.

Supporting Information

Acknowledgements

Conflict of Interest

The authors declare no conflict of interest.

Keywords

[1] M. Hartmann, W. Schwieger, *Chem. Soc. Rev.* **2016**, *45*, 3311.
[2] R. Lakers, *Nature* **1993**, *361*, 511.
[3] W. G. Bae, H. N. Kim, D. Kim, S. H. Park, H. E. Jeong, K.-Y. Suh, *Adv. Mater.* **2014**, *26*, 675.
[4] M.-H. Sun, S.-Z. Huang, L.-H. Chen, Y. Li, X.-Y. Yang, Z.-Y. Yuan, B.-L. Su, *Chem. Soc. Rev.* **2016**, *45*, 3479.
[5] X. Zhao, P. Pachfule, S. Li, T. Langenhahn, M. Ye, C. Schlesiger, S. Praetz, J. Schmidt, A. Thomas, *J. Am. Chem. Soc.* **2019**, *141*, 6623.
[6] H. Wang, M. Qu, S. Wang, X. Liu, L. Li, *Adv. Sustainable Syst.* **2019**, *3*, 1970013.
[7] W. G. Lim, C. Jo, A. Cho, J. Hwang, S. Kim, J. W. Han, J. Lee, *Adv. Mater.* **2019**, *31*, 1806547.
[8] N. P. Sari, D. Dutta, A. Jamaluddin, J.-K. Change, C.-Y. Su, *Phys. Chem. Chem. Phys.* **2017**, *19*, 30381.
[9] S. Jia, Y. Wang, X. Liu, S. Zhao, W. Zhao, Y. Huang, Z. Li, Z. Lin, *Nano Energy* **2019**, *59*, 229.
[10] H.-W. Liang, X. Zhuang, S. Brüller, X. Feng, K. Müllen, *Nat. Commun.* **2014**, *5*, 4973.
[11] Y. Chen, Y. Lin, Y. Zhang, S. Wang, D. Su, Z. Yang, M. Han, F. Chen, *Nano Energy* **2014**, *8*, 25.
[12] R. L. Thankamony, X. Li, X. Fan, G. Sheng, X. Wang, S. Sun, X. Zhang, Z. Lai, *ACS Appl. Mater. Interfaces* **2018**, *10*, 44041.
[13] Y. Guan, F. Cheng, Z. Pan, *Polymers* **2019**, *11*, 806.
[14] Y. Jiao, S. W. Cho, S. Lee, S. H. Kim, S. Y. Jeon, K. Hur, S. M. Yoon, *Adv. Eng. Mater.* **2018**, *20*, 1700608.
[15] Z. Wang, X. Guan, H. Huang, H. Wang, W. Lin, Z. Peng, *Adv. Funct. Mater.* **2019**, *29*, 1807569.
[16] L. S. Zhong, J. S. Hu, H. P. Liang, A. M. Cao, W. G. Song, L. J. Wan, *Adv. Mater.* **2006**, *18*, 2426.
[17] H. J. Ensikat, P. Ditsche-Kuru, C. Neinhuis, W. Barthlott, *Beilstein J. Nanotechnol.* **2011**, *2*, 152.
[18] J. Jeevahan, M. Chandrasekaran, J. G. Britto, R. B. Durairaj, G. Mageshwaran, *J. Coat. Technol. Res.* **2018**, *15*, 231.
[19] X.-Y. Yang, L.-H. Chen, Y. Li, J. C. Rooke, *Chem. Soc. Rev.* **2017**, *46*, 481.
[20] H. M. Reinhardt, K. Bücker, N. A. Hampp, *Opt. Express* **2015**, *23*, 11965.
[21] H. M. Reinhardt, H.-C. Kim, C. Pietzonka, J. Kruempelmann, B. Harbrecht, B. Roling, N. Hampp, *Adv. Mater.* **2013**, *25*, 3313.
[22] H. Oh, J. Lee, M. Seo, I.-U. Baek, J.-Y. Byun, M. Lee, *ACS Appl. Mater. Interfaces* **2018**, *10*, 38368.
[23] H. M. Reinhardt, C. Hellmann, P. Nürnberger, S. Kachel, N. Hampp, *Adv. Mater. Interfaces* **2017**, *4*, 1700508.
[24] H. M. Reinhardt, C. Pietzonka, B. Harbrecht, N. Hampp, *Adv. Mater. Interfaces* **2014**, *1*, 1300060.
[25] Z. Lui, J. Siegel, M. Garcia-Lechuga, T. Epicier, Y. Lefkir, S. Reynaud, M. Bugnet, F. Vocanson, J. Solis, G. Vitrant, N. Destouches, *ACS Nano* **2017**, *11*, 5031.
[26] A. Y. Vorobyev, C. Guo, *Laser Photonics Rev.* **2013**, *7*, 385.
[27] J. Yong, Q. Yang, C. Guo, F. Chen, X. Hou, *RSC Adv.* **2019**, *9*, 12470.
[28] B. Schumacher, R. Ochs, H. Tröße, S. Schlabach, M. Bruns, D. V. Szabó, J. Haußelt, *Plasma Processes Polym.* **2007**, *4*, S865.
[29] R. Ochs, D. V. Szabó, S. Schlabach, S. Becker, S. Indris, *Phys. Status Solidi A* **2011**, *208*, 471.
[30] N. E. Kask, S. V. Michurin, G. M. Fedorov, *Quantum Electron.* **2003**, *33*, 57.
[31] M. Vlasova, P. A. Márquez Aguilar, M. C. Reséndiz-González, M. Kakazey, V. Stetsenko, T. Tomila, A. Ragulya, *Sci. Sintering* **2008**, *40*, 69.
[32] V. P. Aksenov, V. V. Voronov, G. N. Mikha lova, N. E. Kask, E. G. Leksina, S. V. Michurin, G. M. Fedorov, *Opt. Zh.* **2008**, *75*, 43.
[33] B. B. Mandelbrot, *The Fractal Geometry of Nature*, Freeman, New York **1983**.
[34] S. S. Cross, *Micron* **1994**, *25*, 101.
[35] R. Zahn, M. F. Lagadec, V. Wood, *ACS Energy Lett.* **2017**, *2*, 2452.
[36] S.-H. Kim, *J. Korean Phys. Soc.* **2005**, *46*, 474.
[37] S. Torquato, *Annu. Rev. Mater. Res.* **2002**, *32*, 77.
[38] T. Müllner, K. K. Unger, U. Tallarek, *New J. Chem.* **2016**, *40*, 3993.
[39] M. Kroll, D. Hlushkou, S. Schlabach, A. Höltzel, B. Roling, U. Tallarek, *J. Electrochem. Soc.* **2018**, *165*, A3156.
[40] S. Gheorghiu, M.-O. Coppens, *AIChE J.* **2004**, *50*, 812.
[41] B. Y. Park, R. Zaouk, C. Wang, M. J. Madou, *J. Electrochem. Soc.* **2007**, *154*, P1.
[42] J. Schindelin, I. Arganda-Carreras, E. Frise, V. Kaynig, M. Longair, T. Pietzsch, S. Preibisch, C. Rueden, S. Saalfeld, B. Schmid, J.-Y. Tinevez, D. J. White, V. Hartenstein, K. Eliceiri, P. Tomancak, A. Cardona, *Nat. Methods* **2012**, *9*, 676.
[43] B. Münch, P. Trtik, F. Marone, M. Stampanoni, *Opt. Express* **2009**, *17*, 8567.